SELF-SIMILAR SOLUTIONS FOR WEAK SHOCK REFLECTION

ALLEN M. TESDALL * AND JOHN K. HUNTER †

Abstract. We present numerical solutions of a two-dimensional Riemann problem for the unsteady transonic small disturbance equations that provides an asymptotic description of the Mach reflection of weak shock waves. We develop a new numerical scheme to solve the equations in self-similar coordinates, and use local grid refinement to resolve the solution in the reflection region. The solutions contain a remarkably complex structure: there is a sequence of triple points and tiny supersonic patches immediately behind the leading triple point that is formed by the reflection of weak shocks and expansion waves between the sonic line and the Mach shock. An expansion fan originates at each triple point, thus resolving the von Neumann paradox of weak shock reflection. These numerical solutions raise the question of whether there is an infinite sequence of triple points in an inviscid weak shock Mach reflection.

Key words. weak shock reflection, self-similar solutions, unsteady transonic small disturbance equation, two-dimensional Riemann problems, von Neumann paradox

AMS subject classifications. 65M06, 35L65, 76L05

1. Introduction. Experimental observations of the Mach reflection of weak shock waves off a wedge show a pattern that closely resembles a single Mach reflection, in which the incident, reflected, and Mach shocks meet at a triple point. The von Neumann theory of shock reflection [10, 16] shows that a standard triple point configuration, consisting of three shocks and a contact discontinuity, is impossible for sufficiently weak shocks. This apparent conflict between theory and experiment for weak shock reflection has been a longstanding puzzle, and is often referred to as the triple point, or von Neumann, "paradox" (see §I.17 of [2], for example).

Guderley [8, 9] proposed that there is a supersonic region behind the triple point in a steady weak shock Mach reflection, in which case there is an additional expansion fan at the triple point, resolving the apparent paradox. There was, however, no evidence of a supersonic region or an expansion fan in experimental observations [3, 18, 19] or numerical solutions [5, 20] of weak shock reflections off a wedge, until Hunter and Brio [12] obtained a numerical solution of a shock reflection problem for the unsteady transonic small disturbance equation that contained a supersonic region behind the triple point. The region is extremely small, which is why it had not been detected previously. Subsequently, Zakharian *et al.* [24] found a supersonic region in a numerical solution of a shock reflection problem for the full Euler equations, using local grid refinement near the triple point, for a set of parameter values corresponding to those in [12].

The solutions in [12, 24] are for a single set of parameter values, and they are not sufficiently well resolved to show an expansion fan at the triple point directly, or to show the structure of the flow inside the supersonic region. In this paper, we present high-resolution numerical solutions of the shock reflection problem for the unsteady transonic small disturbance equations for a range of parameter values. There is a

supersonic region behind the triple point in all of the numerical solutions obtained here. This region consists of a sequence of supersonic patches formed by a sequence of expansion fans and shock waves that are reflected between the sonic line and the Mach shock (see Fig. 5 and Fig. 6, for example). Each of the reflected shocks intersects the Mach shock, resulting in a sequence of triple points, rather than a single triple point. The numerical results raise the question of whether there is an infinite sequence of triple points in an inviscid weak shock Mach reflection.

The total size of the repeating structure of supersonic patches is approximately the same as that of the supersonic region in the solution obtained in [12], at the same parameter value, by a different numerical scheme. Other important quantities, including the strength of the reflected shock and the location of the triple point, agree closely with this solution, providing an independent check on the self-similar solutions presented here.

There are, at the moment, no experimental observations of a supersonic region behind the triple point in a weak shock Mach reflection. As we discuss in §5, the small size of the region and the effect of viscosity may make it very difficult to detect experimentally. A similar structure to the one in the solutions presented here has been observed in shock-boundary layer interactions in transonic flows over an airfoil [1, 13] (see Fig. 245 and Fig. 247 in [6]). The shock reflects off a laminar boundary layer as an expansion wave, leading to a sequence of reflected shock and expansion waves inside the supersonic bubble on the airfoil.

The numerical solutions of weak shock reflection in [5, 12, 20, 24] were obtained by solving an initial-value problem for the unsteady equations. The problem of inviscid shock reflection off a wedge is self-similar, and there are a number of advantages to solving the problem in self-similar, rather than unsteady, form. In the unsteady formulation the equations are time-marched, and any waves present move through the computational domain, complicating algorithms for local grid refinement near the triple point. By contrast, a solution of the self-similar equations is stationary, making local grid refinement algorithms much easier to implement. Moreover, a global grid refinement strategy is possible, in which a partially converged solution on a coarse grid is interpolated onto a fine grid, and then converged on the fine grid. This process may be repeated recursively until the desired resolution is obtained.

In this paper, we present numerical solutions of the shock reflection problem for the unsteady transonic small disturbance equations computed in self-similar coordinates. Samtaney [17] developed a scheme for the solution of the Euler equations in self-similar coordinates, but his scheme does not apply to the unsteady transonic small disturbance equations, and a different approach is required. In our approach, we introduce special self-similar variables in which the self-similar transonic small disturbance equations have the form of the usual transonic small disturbance equations modified by lower order terms. What makes the use of the unsteady transonic small disturbance equations worthwhile is the fact that, with the same computational resources, we can obtain a much more finely resolved solution than for the Euler equations.

This paper is organized as follows. In §2, we describe the shock reflection problem for the unsteady transonic small disturbance equation, and in §3 we give the details of our numerical method. In §4, we present our numerical solutions. In §5, we discuss some of the questions raised by these solutions, and consider the effect of physical viscosity on the inviscid solutions. We summarize our conclusions in §6.

2. The asymptotic shock reflection problem. The asymptotic shock reflection problem [11, 12, 14, 20] consists of the unsteady transonic small disturbance

equation

$$u_t + \left(\frac{1}{2}u^2\right)_x + v_y = 0, \tag{2.1}$$
$$u_y - v_x = 0,$$

in the half space $y > 0$ with the initial and boundary conditions

$$u(x, y, 0) = \begin{cases} 0 & \text{if } x > ay, \\ 1 & \text{if } x < ay, \end{cases} \tag{2.2}$$

$$v(x, y, t) = 0 \qquad \text{if } x > \sigma(y, t), \tag{2.3}$$

$$v(x, 0, t) = 0. \tag{2.4}$$

Here, $x = \sigma(y, t)$ is the location of the incident and Mach shocks. The location of the incident shock is given by

$$x = ay + \left(\frac{1}{2} + a^2\right)t. \tag{2.5}$$

The incident shock strength, as measured by the jump in u, is normalized to one. This problem depends on a single parameter a, the inverse slope of the incident shock.

These equations may be derived by a systematic asymptotic expansion of the shock reflection problem for the full Euler equations for weak shock reflection off thin wedges [12]. The variables $u(x, y, t)$, $v(x, y, t)$ are proportional to the x, y fluid velocity components, respectively, and pressure perturbations are proportional to u. The flow is irrotational and isentropic to leading order in the shock strength.

If the Mach number of the incident shock is M, and the wedge angle in radians is θ_w, then (2.1)–(2.4) is obtained in the limit $M \to 1$ and $\theta_w \to 0$, with

$$a = \frac{\theta_w}{2\sqrt{M - 1}} \tag{2.6}$$

fixed. Because of transonic similarity, the asymptotic problem depends on a single combination of the incident shock strength and the wedge angle. A regularly reflected solution of (2.1)–(2.4) is impossible when $a < \sqrt{2}$, and triple point solutions of (2.1), in which three plane shocks separated by constant states meet at a point, do not exist.

The problem (2.1)–(2.4) is self-similar, so the solution depends only on the similarity variables

$$\xi = \frac{x}{t}, \qquad \eta = \frac{y}{t}.$$

Writing (2.1) in terms of ξ, η, and a pseudo-time variable $\tau = \log t$, we get

$$u_\tau - \xi u_\xi - \eta u_\eta + \left(\frac{1}{2}u^2\right)_\xi + v_\eta = 0, \tag{2.7}$$
$$u_\eta - v_\xi = 0.$$

As $\tau \to +\infty$, solutions of (2.7) converge to a pseudo-steady, self-similar solution that satisfies

$$-\xi u_\xi - \eta u_\eta + \left(\frac{1}{2}u^2\right)_\xi + v_\eta = 0, \tag{2.8}$$
$$u_\eta - v_\xi = 0.$$

Equation (2.8) is hyperbolic when $u < \xi + \eta^2/4$, corresponding to supersonic flow in a self-similar coordinate frame, and elliptic when $u > \xi + \eta^2/4$, corresponding to subsonic flow. The equation changes type across the sonic line given by

$$\xi + \frac{\eta^2}{4} = u(\xi, \eta). \tag{2.9}$$

3. The numerical method. In order to solve (2.7) numerically, we write it in terms of parabolic coordinates

$$r = \xi + \frac{1}{4}\eta^2, \qquad \theta = \eta, \tag{3.1}$$

$$\widetilde{u} = u - \left(\xi + \frac{1}{4}\eta^2\right), \qquad \widetilde{v} = v - \frac{1}{2}\eta u,$$

which gives

$$\widetilde{u}_\tau + \left(\frac{1}{2}\widetilde{u}^2\right)_r + \widetilde{v}_\theta + \frac{3}{2}\widetilde{u} + \frac{1}{2}r = 0, \tag{3.2}$$

$$\widetilde{u}_\theta - \widetilde{v}_r = 0.$$

With respect to these variables, the self-similar equations have the form of the usual transonic small disturbance equations modified by lower-order terms, and they can be solved by a standard numerical scheme. We introduce a potential $\varphi(r, \theta, \tau)$ such that

$$\widetilde{u} = \varphi_r, \qquad \widetilde{v} = \varphi_\theta, \tag{3.3}$$

and write (3.2) in the potential form

$$\varphi_{r\tau} + \left(\frac{1}{2}\varphi_r^2\right)_r + \varphi_{\theta\theta} + \frac{3}{2}\varphi_r + \frac{1}{2}r = 0. \tag{3.4}$$

We define a non-uniform grid r_i in the r direction and θ_j in the θ direction, where $r_{i+1} = r_i + \Delta r_{i+1/2}$ and $\theta_{j+1} = \theta_j + \Delta\theta_{j+1/2}$. We also define $(r_{i-1/2}, r_{i+1/2})$ as the neighborhood of the point r_i, with length $\Delta r_i = \frac{1}{2}(\Delta r_{i-1/2} + \Delta r_{i+1/2})$, where $r_{i+1/2} = \frac{1}{2}(r_{i+1} + r_i)$. Similar definitions apply for the non-uniform grid θ_j. We denote an approximate solution of (3.4) by

$$\varphi_{i,j}^n \approx \varphi(r_i, \theta_j, n\Delta\tau),$$

where $\Delta\tau$ is a fixed time step, and discretize (3.4) in time τ using

$$\frac{\varphi_r^{n+1} - \varphi_r^n}{\Delta\tau} + \varphi_{\theta\theta}^{n+1} + f(\varphi_r)_r^n + \frac{3}{2}\varphi_r^{n+1} + \frac{1}{2}r = 0, \tag{3.5}$$

where the flux function f is defined by

$$f(\widetilde{u}) = \frac{1}{2}\widetilde{u}^2. \tag{3.6}$$

We solve (3.5) by sweeping from right to left in r, using the spatial discretization

$$\varphi_{i,j}^{n+1} - \Delta r_{i+1/2}\Delta\tau \left(\frac{\frac{\varphi_{i,j+1}-\varphi_{i,j}}{\Delta\theta_{j+1/2}} - \frac{\varphi_{i,j}-\varphi_{i,j-1}}{\Delta\theta_{j-1/2}}}{\Delta\theta_j}\right)^{n+1} + \frac{3}{2}\Delta\tau\varphi_{i,j}^{n+1} \tag{3.7}$$

$$= \varphi_{i+1,j}^{n+1} - \varphi_{i+1,j}^n + \varphi_{i,j}^n + \Delta\tau \left(F(\widetilde{u}_{i+1/2,j}, \widetilde{u}_{i+3/2,j})^n - F(\widetilde{u}_{i-1/2,j}, \widetilde{u}_{i+1/2,j})^n\right)$$

$$+ \frac{3}{2}\Delta\tau\varphi_{i+1,j}^{n+1} + \frac{1}{2}\Delta\tau\Delta r_{i+1/2}\, \hat{r}_{i+1/2}.$$

Here, F is a numerical flux function, and

$$\widetilde{u}_{i-1/2,j} = \frac{\varphi_{i,j} - \varphi_{i-1,j}}{\Delta r_{i-1/2}}.$$

The variable $\hat{r}_{i+1/2}$ is the value of r at which the source term $\frac{1}{2}r$ is evaluated, and in most of the calculations we used the definition $\hat{r}_{i+1/2} = r_i$. We tried a number of different treatments of the source term and obtained similar results with them all. See [21] for a detailed discussion.

In most of the computations, we used an Engquist-Osher numerical flux function. Dropping the θ-subscript j, which is constant in the following definitions, the Engquist-Osher flux for (3.6) is

$$F^{EO}(\widetilde{u}_{i-1/2}, \widetilde{u}_{i+1/2}) = \frac{1}{2}\max(\widetilde{u}_{i-1/2}, 0)^2 + \frac{1}{2}\min(\widetilde{u}_{i+1/2}, 0)^2.$$

In our highest resolution computations for $a = 0.5$, we used a second-order, flux-limiter scheme [23], with a Lax-Wendroff flux as the higher-order flux, and an Engquist-Osher flux as the lower-order flux. The numerical flux function for this scheme is given by

$$F(\widetilde{u}_{i-1/2}, \widetilde{u}_{i+1/2}) = \psi(\varrho)F^{LW}(\widetilde{u}_{i-1/2}, \widetilde{u}_{i+1/2}) + (1 - \psi(\varrho))F^{EO}(\widetilde{u}_{i-1/2}, \widetilde{u}_{i+1/2}),$$

$$\varrho = \begin{cases} \dfrac{\left(\left|\frac{\widetilde{u}_{i-3/2}+\widetilde{u}_{i-1/2}}{2}\right| - \frac{\Delta\tau}{\Delta r_i}\left(\frac{\widetilde{u}_{i-3/2}+\widetilde{u}_{i-1/2}}{2}\right)^2\right)(\widetilde{u}_{i-1/2}-\widetilde{u}_{i-3/2})}{\left(\left|\frac{\widetilde{u}_{i-1/2}+\widetilde{u}_{i+1/2}}{2}\right| - \frac{\Delta\tau}{\Delta r_i}\left(\frac{\widetilde{u}_{i-1/2}+\widetilde{u}_{i+1/2}}{2}\right)^2\right)(\widetilde{u}_{i+1/2}-\widetilde{u}_{i-1/2})}, & \frac{\widetilde{u}_{i-1/2}+\widetilde{u}_{i+1/2}}{2} \geq 0 \\[30pt] \dfrac{\left(\left|\frac{\widetilde{u}_{i+1/2}+\widetilde{u}_{i+3/2}}{2}\right| - \frac{\Delta\tau}{\Delta r_i}\left(\frac{\widetilde{u}_{i+1/2}+\widetilde{u}_{i+3/2}}{2}\right)^2\right)(\widetilde{u}_{i+3/2}-\widetilde{u}_{i+1/2})}{\left(\left|\frac{\widetilde{u}_{i-1/2}+\widetilde{u}_{i+1/2}}{2}\right| - \frac{\Delta\tau}{\Delta r_i}\left(\frac{\widetilde{u}_{i-1/2}+\widetilde{u}_{i+1/2}}{2}\right)^2\right)(\widetilde{u}_{i+1/2}-\widetilde{u}_{i-1/2})}, & \frac{\widetilde{u}_{i-1/2}+\widetilde{u}_{i+1/2}}{2} < 0, \end{cases}$$

where ψ is a minmod flux-limiter,

$$\psi(\varrho) = \begin{cases} 0, & \varrho \leq 0, \\ \varrho, & 0 < \varrho < 1, \\ 1, & \varrho \geq 1. \end{cases}$$

The Lax-Wendroff flux for (3.6) is given by

$$F^{LW}(\widetilde{u}_{i-1/2}, \widetilde{u}_{i+1/2}) = \frac{1}{4}(\widetilde{u}_{i-1/2}^2 + \widetilde{u}_{i+1/2}^2)$$
$$- \frac{1}{2}\frac{\Delta\tau}{\Delta r_i}\left(\frac{\widetilde{u}_{i-1/2} + \widetilde{u}_{i+1/2}}{2}\right)^2(\widetilde{u}_{i+1/2} - \widetilde{u}_{i-1/2}).$$

We evolve the solution of (3.7) forward in time τ until it converges to a steady state, using line relaxation. The direction of sweep, from right to left in r, is consistent with the direction of propagation of the characteristics for (2.8), which is in the $-r$ direction.

3.1. Boundary conditions. We computed solutions of the half-space problem (2.1)–(2.4) in the finite computational domain

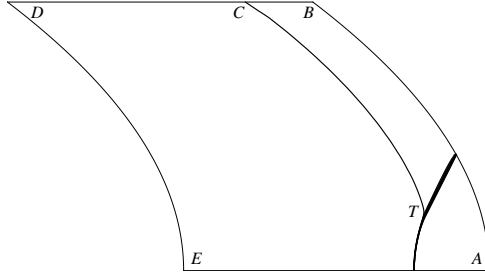$$r^L \leq r \leq r^R, \qquad 0 \leq \theta \leq \theta^T,$$

FIG. 1. *A schematic diagram of the computational domain. EA is the wall and ABDE is the numerical boundary. The incident shock enters the computational domain through AB. The incident, reflected, and Mach shocks meet at the triple point T.*

shown schematically in Figure 1. The left and right boundaries of the computational domain are parabolic because of the use of the coordinates in (3.1). We use a nonuniform grid that has a locally refined area of uniform grid very close to the triple point, and is stretched exponentially away from the triple point toward the outer numerical boundaries and the wall. In the solutions shown below, the nonuniform grids are stretched by amounts between 0.5% and 1.5%, and the total number of grid points in our largest grid is approximately 3×10^6.

We impose the physical no-flow condition (2.4), which implies that $\varphi_\theta = 0$, on the wall EA. In addition, we require numerical boundary conditions on the outer computational boundaries.

On the right boundary AB, we impose Dirichlet data corresponding to the incident shock solution in (2.2)–(2.3). Using (3.1) in (2.5), we find that the incident shock location with respect to the transformed self-similar coordinates is given by

$$r = a\theta + \frac{1}{4}\theta^2 + \frac{1}{2} + a^2.$$

Thus, the incident shock location is a parabola with respect to the transformed coordinates, instead of a straight line. Ahead of the incident shock we have $(u, v) = (0, 0)$, and behind the incident shock we have $(u, v) = (1, -a)$. Hence, using (3.1), (3.3), and the requirement that the potential is continuous across the shock, we find that the potential for the incident shock solution is given by

$$\varphi(r, \theta) = \begin{cases} -\frac{1}{2}r^2, & r > a\theta + \frac{1}{4}\theta^2 + \frac{1}{2} + a^2, \\ r - a\theta - \frac{1}{4}\theta^2 - \frac{1}{2}r^2 - \frac{1}{2} - a^2, & r < a\theta + \frac{1}{4}\theta^2 + \frac{1}{2} + a^2. \end{cases} \qquad (3.8)$$

We impose (3.8) as a boundary condition for (3.4) on AB.

The asymptotic behavior of the solution of the shock reflection problem at large distances from the reflection point is given by the solution of the linearized shock reflection problem [12]. We use this result to formulate a numerical boundary condition on the subsonic boundary CDE. In self-similar variables, the linearized solution for φ_r behind the reflected wavefront $r = 1$ is

$$\varphi_r = 1 - r + \frac{1}{\pi} \tan^{-1} \left(\frac{2a\sqrt{1-r}}{1 - r + \frac{1}{4}\theta^2 - a^2} \right), \quad r < 1. \qquad (3.9)$$

We impose (3.9) as a Neumann condition on the left boundary DE. Writing (3.9) as

$\varphi_r = f(r, \theta)$, we discretize it as

$$\frac{\varphi_{i+1,j} - \varphi_{i,j}}{\Delta r_{i+1/2}} = f(r_{i+1/2}, \theta_j).$$

On the top boundary BD, we impose the Dirichlet condition (3.8) when $r > 1$, corresponding to the segment BC, and the condition (3.9) when $r < 1$, corresponding to the segment CD. The exact location of the reflected shock is slightly different from the point $r = 1$, where we switch the numerical boundary conditions, and the exact solution differs slightly from the linearized solution, but we found that the disturbance originating from the top boundary was small provided that the boundary was far enough away from the triple point (see Fig. 9). We tried a number of other numerical boundary conditions, but (3.8)–(3.9) gave the most satisfactory results.

4. Numerical results. We computed numerical solutions of (2.1)–(2.4) for a equal to 0.3, 0.4, 0.5, 0.6, 0.65, 0.7, 0.75, and 0.8. In the following figures, we present solutions for the values 0.3, 0.5, 0.6, and 0.8. The solutions for the other values of a are similar to the ones presented here. Fig. 2 shows u-contour plots of the global solutions as a function of $(x/t, y/t)$. From (2.6), increasing a corresponds to increasing the wedge angle while fixing the Mach number of the incident shock, or decreasing the Mach number while fixing the wedge angle. Hence, the sequence of plots in Fig. 2(a)–(d) is a numerical representation of a series of shock reflection experiments in which the wedge angle is increased, while the Mach number is held constant at a value near one.

The numerical solutions closely resemble a single Mach reflection. The Mach shock becomes shorter and stronger as a increases, and the strength of the reflected shock near the triple point, which is very weak for smaller values of a, also increases with a (see Table 4.1). For a fixed value of a, the strength of the Mach shock increases as it moves away from the triple point, reaching a maximum at the wall $y = 0$. The strength of the reflected shock increases initially as it moves away from the triple point, then decreases, approaching zero as $y \to +\infty$. The thickening of the incident shock as it moves away from the triple point in Fig. 2(a)–(d) is caused by the use of a stretched grid.

In Fig. 3, we show the u-contours and the numerically computed location of the sonic line (2.9) near the triple point for the values of a shown in Fig. 2. All of the solutions contain a small region of supersonic flow behind the triple point, the size of which decreases rapidly with increasing a. Table 4.1 gives the size of the supersonic region in the numerical solution for each value of a. The height $\Delta(y/t)$ is a numerical estimate of the difference between the maximum value of y/t on the sonic line and the minimum value of y/t at the rear sonic point on the Mach shock. The width $\Delta(x/t)$ is an estimate of the width of the supersonic region at the value of y/t corresponding to the triple point. In detailed plots of our most refined solution with $a = 0.5$ (see Fig. 5 and Fig. 6, for example), the expansion fan generated by the collision of the reflected shock with the incident shock at the triple point can be clearly seen. Behind the leading triple point, there is a sequence of shocks and expansion fans. These shocks are less apparent in the less resolved solutions, such as Fig. 3(c), and in Fig. 3(d) they cannot be seen at all.

The area covered by the most refined uniform grid fits inside the region shown in Fig. 3(a)–(d); the actual refined grid area would appear as a sheared rectangle because the equations are discretized with respect to the parabolic coordinates in (3.1). The figure caption gives the number of grid points in the most refined area of the grid.

TABLE 4.1
Numerically computed values of the size of the supersonic region at the triple point, the triple point location, and the strength $[u]_r$ of the reflected shock at the sonic point. The shock strength is measured by the jump $[u]$ in u.

a	$\Delta(x/t)$	$\Delta(y/t)$	$(x/t)_{t.p.}$	$(y/t)_{t.p.}$	$[u]_r$
0.3	0.0030	0.023	0.837	0.831	0.01
0.4	0.0023	0.019	0.924	0.665	0.03
0.5	0.0012	0.0096	1.008	0.513	0.07
0.6	0.0006	0.0030	1.098	0.398	0.13
0.65	0.0004	0.0014	1.148	0.349	0.17
0.7	0.00016	0.00074	1.200	0.302	0.22
0.75	0.00008	0.00027	1.255	0.258	0.27
0.8	0.00004	0.00011	1.315	0.220	0.33

The small numerical oscillations immediately behind the Mach shock (see Fig. 3(a) and (d), for example) seem to be caused by the lack of alignment of the shock with the grid.

We found that, for a given value of a, a certain minimum grid resolution was required to resolve the supersonic region behind the triple point. As we refined the grid beyond this minimum level, a detailed flowfield structure in the region emerged. Fig. 4 shows the u-contours and the sonic line near the triple point for a sequence of solutions for $a = 0.5$ computed on successively refined grids. In this sequence, we refined each grid by a factor of two in x/t and y/t in relation to the previous grid. The resolution of the locally refined areas is indicated on the plots. In Fig. 4(a)–(b), the sonic line appears fairly smooth. The supersonic region in Fig. 4(b) is similar in size, shape, and resolution to the one obtained in [12]. At the next level of refinement, shown in Fig. 4(c), there is an indication of the coalescence of u-contours at the rear of the supersonic region, and evidence of a second reflected shock there. Finally, in Fig. 4(d), the second reflected shock is better defined, with an indication of a third, weaker shock following it. Further shocks appear in our most refined solution in Fig. 3(b).

Returning to Fig. 3, we can explain the qualitative differences between the solutions for different values of a in terms of their numerical resolution. As shown in Table 4.1, the size of the supersonic region decreases with increasing a. We therefore had to use more refined grids for higher values of a. For example, the solution shown in Fig. 3(d) for $a = 0.8$ was computed using a grid that was a factor of 16 times more refined in x/t and y/t than the grid used in the solution for $a = 0.5$ shown in Fig. 3(b). However, the supersonic region in Fig. 3(d) is smaller than the one in Fig. 3(b) by a linear factor of about 90, resulting in a lower relative resolution. Consequently, the detailed flowfield near the triple point is not visible in Fig. 3(d), similar to the under-resolved solutions shown in Fig. 4(a)–(b). By contrast, the solutions for $a = 0.3, 0.5, 0.6$ in Fig. 3(a)–(c) contain a sequence of shocks and expansions, evident from the pronounced bumps in the sonic line.

There is a small discrepancy between the numerically computed location of the triple point in these figures and the theoretical location of the incident shock in (2.5). The reason for this discrepancy is that the numerical boundary conditions did not give an incident shock that was of exactly constant strength and exactly straight in $(x/t, y/t)$-coordinates. The deviation of the numerical solution for the incident shock from the exact uniform solution was, however, very small. For example, in our numerical solution for $a = 0.5$, the nonuniformity in u and v in the state behind

the incident shock is less than 0.4%, and the numerically computed value of the x/t-coordinate of the triple point differs by 0.15% from the theoretical value obtained from (2.5) using the numerically computed value of y/t. We tried a number of different implementations of the numerical scheme and boundary conditions, but none of them gave an exactly straight incident shock. Nevertheless, we saw a supersonic region and the same structure of reflected shocks and expansion fans inside it for all of the implementations.

In Fig. 5, we plot closely spaced u-contours, and more widely spaced v-contours, to give a detailed picture of the sequence of shock and expansion waves for $a = 0.5$. Fig. 6 is an enlargement of the solution shown in Fig. 5 over a very small area close to the leading triple point, which shows the expansion wave that originates at the triple point. The expansion wave is in the opposite family to the shock waves, and it reflects off the sonic line as a compression wave (*cf.* the discussion in [9]). This compression wave forms a shock that hits the Mach shock, and reflects as the next expansion wave. The result is a sequence of triple points, rather than a single triple point. The variables u and v decrease smoothly across the expansion wave at the front of a patch from sonic to supersonic values, moving from right to left in the downstream direction; then u and v jump from supersonic to subsonic values across the shock at the rear of a patch. A very weak wave is visible behind the incident shock in Fig. 5(b). This wave is a numerical artifact that is generated when the incident shock crosses from the stretched grid into the uniform grid.

Each shock-expansion pair in the sequence is smaller and weaker than the one preceding it. Four reflected shocks appear to be visible in Figs. 5–6. From the numerical data, their approximate strengths, beginning with the leading reflected shock, are

$$[u]_1 \approx 0.08, \qquad [u]_2 \approx 0.02, \qquad [u]_3 \approx 0.01, \qquad [u]_4 \approx 0.003.$$

Here, the jump $[u]$ in u across a reflected shock is measured at the point where the flow behind the shock is sonic. This point is very close to the corresponding triple point on the Mach shock, as shown in Fig. 6. It is not possible, however, to determine from the numerical solution whether or not this sonic point coincides exactly with the triple point, as argued by Guderley [9] in the case of steady weak shock Mach reflections.

Three shocks and an expansion fan appear to connect four states at the leading triple point. We label these states 1–4 in Fig. 6. Table 4.2 gives values of u and v for each of the states, computed from the numerical solution. For states 2–4, these values were computed at the locations indicated in the figure. The values of (u, v) for state 3 behind the reflected shock were computed close to the point where the flow behind the shock is sonic. This ensures that states 2 and 3 are connected by the reflected shock, and not by any part of the expansion fan, which connects states 3 and 4. For state 1, the values for (u, v) were computed at a location sufficiently far ahead of the incident shock that they were not influenced by the effects of numerical diffusion near the shock.

The velocity components $(\bar{u}, \bar{v})$ in a reference frame moving with the triple point are given by [12]

$$\bar{u} = u - \left(\xi_* + \frac{1}{4}\eta_*^2 \right), \qquad \bar{v} = v - \frac{1}{2}\eta_* u, \qquad (4.1)$$

where (ξ_*, η_*) are the (ξ, η) coordinates of the triple point. From the numerical solution shown in Fig. 6, we obtain $\xi_* = 1.008$, $\eta_* = 0.5128$. We show the corresponding

TABLE 4.2

Numerically computed values for the four states at the leading and second triple points, from the solution for $a = 0.5$ (see Fig. 6). The state ahead of the incident shock is denoted by 1, the state behind the incident shock by 2, the state behind the reflected shock by 3 and the state behind the Mach shock by 4. The states $1'-4'$ are the four analogous states at the second triple point. The variables $\bar{u}$ and $\bar{v}$ are defined in (4.1), with $\xi_* = 1.008$, $\eta_* = 0.5128$ for states 1–4, corresponding to the leading triple point, and $\xi_* = 1.007$, $\eta_* = 0.5108$ for states $1'-4'$, corresponding to the second triple point.

State	u	v	$\bar{u}$	$\bar{v}$
1	0	0	-1.074	0
2	0.997	-0.5000	-0.077	-0.756
3	1.073	-0.4963	-0.001	-0.771
4	1.047	-0.5062	-0.027	-0.775
$1'$	0	0	-1.072	0
$2'$	1.052	-0.5076	-0.020	-0.776
$3'$	1.072	-0.5047	0.000	-0.778
$4'$	1.060	-0.5088	-0.012	-0.779

values of $(\bar{u}, \bar{v})$ in Table 4.2. In Fig. 7(a), we plot the shock and rarefaction curves for the steady transonic small disturbance equation [12] through each of the four states for $(\bar{u}, \bar{v})$. The plot in Fig. 7(b) is an enlarged view of the shock and rarefaction curves for the states 2, 3, and 4. The curves coincide almost exactly with those of a triple point with an expansion fan. We show similar curves through the numerical values of the analogous states at the second triple point in Fig. 7(c)–(d). These plots show that the triple points with expansion fans that we observe numerically are consistent with theory.

To accelerate the convergence of the solution on a very refined grid, we partially converged the solution on a coarse grid, interpolated the solution onto a refined grid, and repeated this process until the desired resolution was obtained. For example, Fig. 4 shows a sequence of solutions obtained on four consecutive intermediate grids during the computation for $a = 0.5$. In Fig. 8, we plot the maximum norm of the residual for a typical computation, in which nine grids were used. The sharp local peaks correspond to interpolations onto more refined grids. In the computation shown, the solution on each intermediate grid was converged until the maximum norm of the residual was less than 10^{-7}. The solution on the final grid in a computation was converged until no further change was observed in the details of the solution near the triple point, which typically occurred when the maximum norm of the residual was less than 10^{-9}.

We performed checks to determine the sensitivity of the solutions to the placement of the top and left numerical boundaries, which intersect the region where (2.8) is elliptic. In Fig. 9, we plot u contours for two solutions for $a = 0.5$ computed on different sized domains. In this study, the top and left numerical boundaries of the smaller domain were extended, as indicated in the figure, to approximately double the distance from these boundaries to the triple point. The contour lines are plotted at the same values of u for both solutions, with the dashed lines representing the u-contours of the solution on the larger domain. The contour lines approach each other, and almost coincide near the triple point.

Fig. 10 is an enlargement of the solutions near the triple point, showing u-contours and v-contours for the solutions on the larger and smaller domains. The u-contours in Fig. 10(a)–(b) and the v-contours in Fig. 10(c)–(d) are plotted at the same values of u and v, respectively, and the sizes of the regions shown in these plots are the same. The

dashed line in Fig. 10(a)–(d) is the sonic line. The structure of reflected shocks and expansion waves, supersonic patches, and repeating triple points, did not change as a result of enlarging the computational domain, and the size of the supersonic region is nearly identical for the two solutions. The main effect of extending the boundaries is a slight shift in the location of the leading triple point. The shift is approximately 0.05% in x/t, and 0.2% in y/t.

5. Discussion. These numerical results raise the question of whether there is an infinite sequence of triple points in an inviscid weak shock Mach reflection. Gamba *et. al.* [7] prove, under some mild assumptions, that the flow behind a triple point cannot be strictly subsonic for the unsteady transonic small disturbance equation. Therefore, if there were a finite sequence of supersonic triple points, there would presumably have to be a smooth transition from supersonic to subsonic flow at the rear of the final supersonic patch. Such a smooth transition appears unlikely to occur, however, because the resulting nonlinear mixed-type boundary value problem would be overdetermined [9, 15].

The most plausible alternative to a finite sequence of triple points terminated by a shock-free supersonic patch is an infinite sequence of more closely spaced triple points, weaker shock-expansion pairs, and smaller supersonic patches that accumulate at the rear sonic point of the supersonic region on the Mach shock. In this structure, the shock and expansion waves would reflect back and forth infinitely many times between the Mach shock and the sonic line, into the rear sonic point. The inviscid equations do not define a length scale so solutions may, in principle, develop arbitrarily small structures. We do not know, however, of a way to confirm or deny the existence of an infinite sequence of patches whose size shrinks to zero.

A remarkable feature of the numerical solutions is the extraordinarily small size of the supersonic region, especially for larger values of a. For example, when $a = 0.8$ the height of the supersonic region is approximately 0.05% of the height of the Mach shock. Once the inverse shock slope a is fixed, there are no further parameters in the problem, so the small size of the region cannot be explained by the dependence of the solution on a small parameter. The shock reflection pattern is produced by the requirement that the y-velocity component v, which is equal to $-a$ behind the incident shock, must return to zero at the wall $y = 0$. Thus, a global scale for v_η is

$$\alpha = \frac{a}{(y/t)_{\text{t.p.}}},$$

where $(y/t)_{\text{t.p.}}$ is the (y/t)-location of the triple point. The supersonic region is produced by the expansion fan that is formed when the leading reflected shock collides with the incident shock. If Δv is the change in v across this fan, then a local scale for v_η near the triple point is

$$\beta = \frac{\Delta v}{\Delta(y/t)},$$

where $\Delta(y/t)$ is the height of the supersonic region. From the numerical data, we find that α is much less than β for larger values of a, corresponding to a rapid change in the solution near the triple point, and a tiny supersonic region. For example, when $a = 0.5$ we find from the numerical data that $\alpha/\beta \approx 1.0$, but when $a = 0.8$ we find that $\alpha/\beta \approx 0.05$. Since the largest value of a that we investigated is 0.8, we do not know if solutions for higher values of a contain a supersonic region with a sequence

of triple points over the entire range $0.8 < a < \sqrt{2}$, nor do we know if the transition between regular and Mach reflection occurs exactly at $a = \sqrt{2}$.

A repeating structure of supersonic patches and triple points with expansion fans appears to provide a resolution of von Neumann's triple point paradox within the framework of inviscid shock theory, and viscosity is not required to explain the structure of a weak shock Mach reflection. Nevertheless, in view of the extremely small size of the supersonic region, it is important to consider the likely effect of physical viscosity on the inviscid description. Since the triple point lies in the interior of the fluid, it is reasonable to expect that boundary layer effects do not influence the local structure of the solution. Thus, the main effect of viscosity is to thicken the shocks. If the size of the supersonic region is smaller than the viscous thickness of the reflected shock, then the sonic line is embedded inside the viscous profile of the reflected shock, and the local structure of the solution near the triple point is dominated by viscous effects. Since the numerical scheme includes numerical viscosity, which mimics the effect of physical viscosity, the plots in Fig. 4 of the solution with increasing numerical resolution presumably indicate the effect of decreasing physical viscosity on the solution. At lower resolutions than the ones shown in Fig. 4, the supersonic region disappears completely, and the sonic line runs down the inside of the reflected shock, through the triple point, and down the Mach shock.

To compare the width of the supersonic region with the viscous shock thickness, we suppose that the reflected shock Mach number is M_r and the mean free path in the gas is λ. The thickness δ of the reflected shock is then given approximately by [22]

$$\delta = \frac{3\lambda}{M_r - 1}.$$

The incident and Mach shocks are thinner than the reflected shock because they are stronger. If the width of the supersonic region in x/t in the solution of the unsteady transonic small disturbance equation is $\Delta(x/t)$, then, from [12], the asymptotic width d of the supersonic region parallel to the wall in physical variables is given by

$$d = 2(M - 1)\Delta(x/t)L.$$

Here, L is the distance traveled by the Mach shock along the wall, from the corner of the wedge to the reflection point, and M is the Mach number of the incident shock. Hence

$$\frac{d}{\delta} = c(M - 1)^2 \frac{L}{\lambda},$$

where the dimensionless constant c is defined by

$$c = \frac{2}{3}\Delta(x/t)[u]_r, \qquad (5.1)$$

and $[u]_r$ is the ratio of the reflected and incident shock strengths,

$$[u]_r = \frac{M_r - 1}{M - 1}.$$

The supersonic region is much larger than the reflected shock structure if $d \gg \delta$, meaning that

$$L \gg \frac{\lambda}{c(M - 1)^2}.$$

The value of c in (5.1) may be estimated from the numerical data in Table 4.1. The supersonic region is easier to observe for larger values of c, and the largest value of c for the results obtained here is $c \approx 6 \times 10^{-5}$ for $a = 0.5$. For smaller values of a, the reflected shock becomes very weak and thick, while for larger values of a, the supersonic region becomes extremely small. The mean free path in argon at standard conditions is approximately $\lambda = 6 \times 10^{-5}$ mm. Therefore, for a shock reflection in argon with $a = 0.5$, we estimate that the supersonic region separates from the viscous profile of the reflected shock when $L \gg (M - 1)^{-2}$ mm. Even for a relatively strong weak shock with $M = 1.1$, this estimate gives $L \gg 100$ mm. Thus, in order to observe the supersonic region in a shock tube experiment, the test section of the tube would have to be significantly longer than 100 mm.

It is striking that such a complex inviscid structure forms on a lengthscale that is comparable with, or less than, the viscous shock thickness in typical experiments.

6. Conclusion. We have presented numerical evidence of a structure of reflected shocks and expansion waves, and a sequence of triple points and supersonic patches, in a tiny region behind the leading triple point of an inviscid weak shock Mach reflection. The presence of the expansion fans at the triple points resolves the von Neumann paradox of weak shock reflection. Qualitative arguments, based on the well-posedness of mixed-type boundary value problems, suggest that there may be an infinite sequence of triple points and patches in an inviscid reflection, but a proof or disproof of this suggestion is lacking. The numerical solutions provide an estimate of the size of the supersonic region, which may enable its experimental detection.

REFERENCES

[1] J. Ackeret, F. Feldmann, and N. Rott, Investigations of compression shocks and boundary layers in fact moving gases, *ETH Report*, number 10, 1946.

[2] G. Birkhoff, *Hydrodynamics*, Revised ed., Princeton University Press, Princeton, 1960.

[3] W. Bleakney and A. H. Taub, Interaction of shock waves, *Rev. Modern Phys.* **21** (1949), pp. 584–605.

[4] M. Brio, and J. K. Hunter, Mach reflection for the two-dimensional Burgers equation, *Physica D*, **60** (1992), pp. 194–207.

[5] P. Colella, and L. F. Henderson, The von Neumann paradox for the diffraction of weak shock waves, *J. Fluid. Mech.*, **213** (1990), pp. 71–94.

[6] M. van Dyke, *An Album of Fluid Motion*, Parabolic Press, Stanford, 1982.

[7] I. M. Gamba, R. R. Rosales, and E. G. Tabak, Constraints on possible singularities for the unsteady transonic small disturbance (UTSD) equations, *Comm. Pure Appl. Math.*, **LII** (1999), pp. 763–779.

[8] K. G. Guderley, Considerations of the structure of mixed subsonic-supersonic flow patterns, Air Materiel Command Tech. Report, F-TR-2168-ND, ATI No. 22780, GS-AAF-Wright Field No. 39, U.S. Wright-Patterson Air Force Base, Dayton, Ohio, October 1947.

[9] K. G. Guderley, *The Theory of Transonic Flow*, Pergamon Press, Oxford, 1962.

[10] L. F. Henderson, Regions and boundaries for diffracting shock wave systems, *Z. Angew. Math. Mech.* **67** (1987), pp. 73–86.

[11] J. K. Hunter, Nonlinear geometrical optics, in *Multidimensional Hyperbolic Problems and Computations*, J. Glimm and A. Majda, eds., IMA Vol. 29, Springer-Verlag, New York, 1991, pp. 179–197.

[12] J. K. Hunter, and M. Brio, Weak shock reflection, *J. Fluid. Mech.*, **410** (2000), pp. 235–261.

[13] H. Liepmann, The interaction between a boundary layer and shock-waves in transonic flow, *Journal of the Aeronautical Sciences*, **13** (1946), pp. 623–637.

[14] C. S. Morawetz, Potential theory for regular and Mach reflection of a shock at a wedge, *Comm. Pure Appl. Math.*, **XLVII** (1994), pp. 593–624.

[15] C. S. Morawetz, The mathematical approach to the sonic barrier, *Bull. Am. Math. Soc.*, **6** (1982), pp. 127–145.

[16] J. von Neumann, *Collected Works*, Vol. 6, Pergamon Press, New York, 1963.

[17] R. SAMTANEY, Computational methods for self-similar solutions of the compressible Euler equations, *J. Comput. Phys.*, **132** (1997), pp. 327–345.

[18] A. SASOH, K. TAKAYAMA, AND T. SAITO, A weak shock wave reflection over wedges, *Shock Waves* **2** (1992), 277–281.

[19] J. STERNBERG, Triple-shock-wave intersections, *Phys. Fluids*, **2** (1959), pp. 179–206.

[20] E. G. TABAK, AND R. R. ROSALES, Focusing of weak shock waves and the von Neumann paradox of oblique shock reflection, *Phys. Fluids*, **6** (1994), pp. 1874–1892.

[21] A. M. TESDALL, Self-similar solutions for weak shock reflection, Ph.D. Thesis, University of California at Davis, 2001.

[22] P. A. THOMPSON, *Compressible Fluid Dynamics*, McGraw-Hill, New York, 1971.

[23] H. Q. YANG, AND A. J. PRZEKWAS, A comparative study of advanced shock-capturing schemes applied to Burgers' equation, *J. Comput. Phys.*, **102** (1992), pp. 139–159.

[24] A. R. ZAKHARIAN, M. BRIO, J. K. HUNTER, AND G. WEBB, The von Neumann paradox in weak shock reflection, *J. Fluid. Mech.*, **422** (2000), pp. 193–205

(a) $a = 0.3$

(b) $a = 0.5$

(c) $a = 0.6$

(d) $a = 0.8$
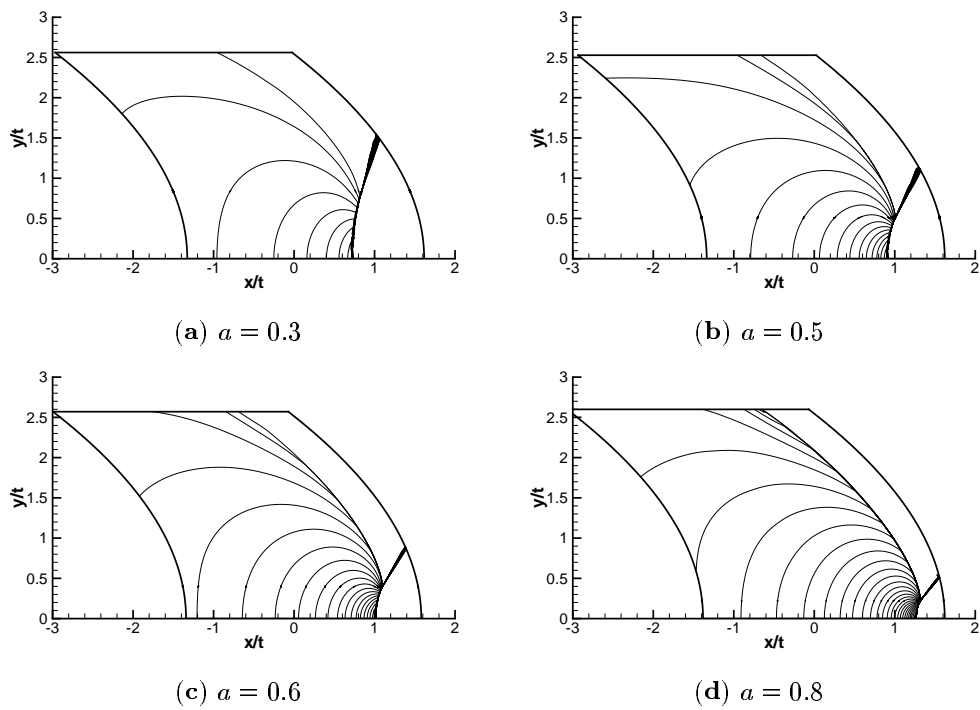
FIG. 2. *Contour plots of u for increasing values of a, showing the full numerical domain. The u−contour spacing is 0.05.*
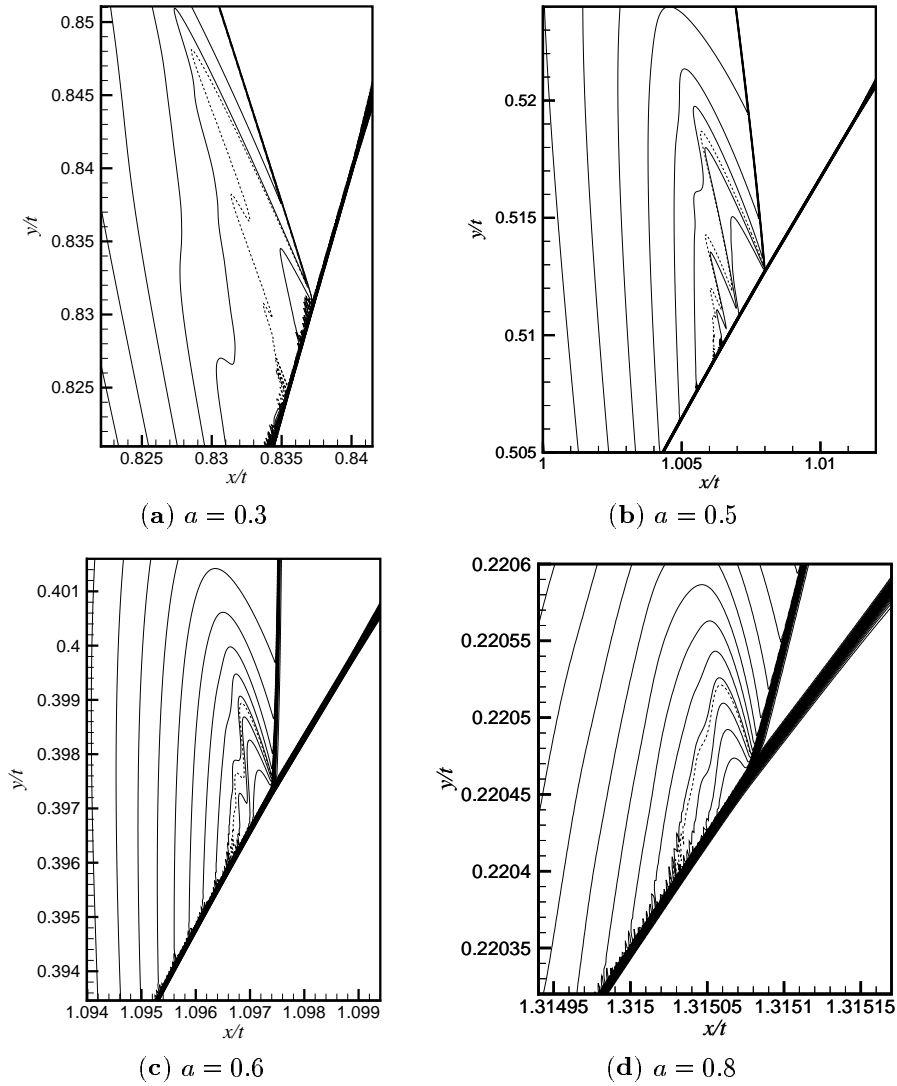
(a) $a = 0.3$

(b) $a = 0.5$

(c) $a = 0.6$

(d) $a = 0.8$

FIG. 3. *Contour plots of u near the triple point for increasing values of a. The u-contour spacing is 0.005 in (a), and 0.01 in (b)–(d). The dotted line is the sonic line. The regions shown contain the refined uniform grids, which have the following numbers of grid points: (a) 620 × 480; (b) 768 × 608; (c) 346 × 260; (d) 245 × 150.*

(a)   **(b)**

(c)   **(d)**
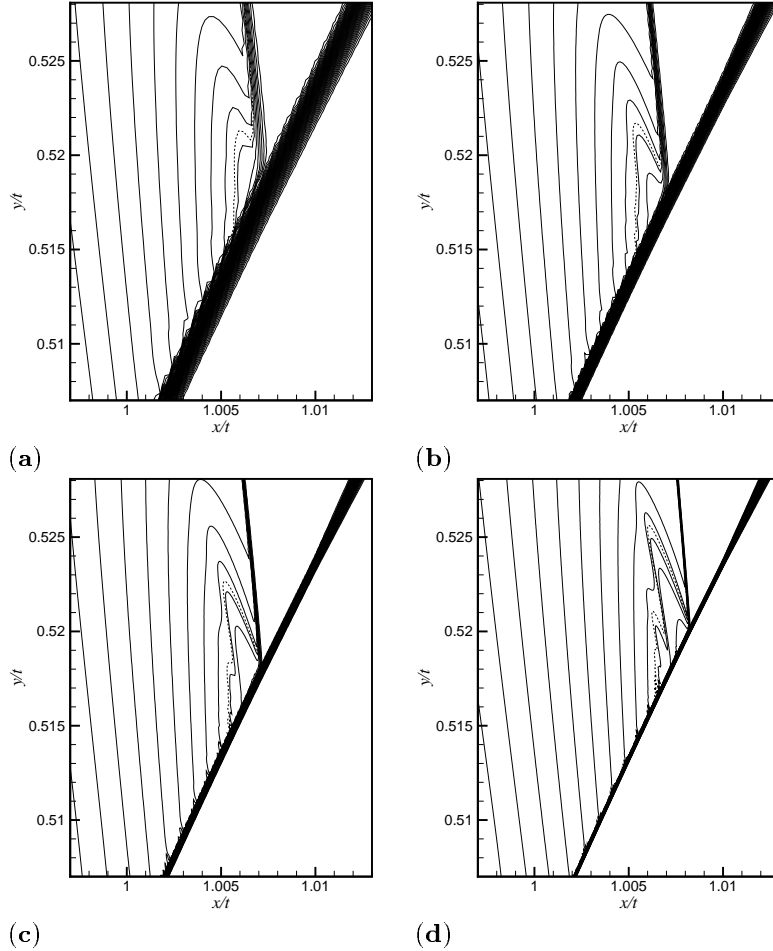
FIG. 4. *A sequence of contour plots illustrating the effect of increasing grid resolution on the numerical solution. The solutions plotted here are for a = 0.5. The figures show the u-contours in the refined grid area near the triple point, with a u-contour spacing of 0.01. Each grid is refined by a factor of two in both x/t and y/t in relation to the previous grid. The region shown includes the refined uniform grid area. The dotted line is the sonic line. In (a), the refined uniform grid contains 64 × 42 grid points. A supersonic region is visible as a bump in the sonic line, but it is poorly resolved. In (b), the refined uniform grid area contains 128 × 84 grid points. The supersonic region appears to be smooth. In (c), the refined uniform grid area contains 256 × 168 grid points. There is an indication of a shock wave behind the leading triple point. The refined uniform grid in (d) contains 512 × 336 grid points. Two shock waves are visible behind the leading triple point.*

(a)   **(b)**
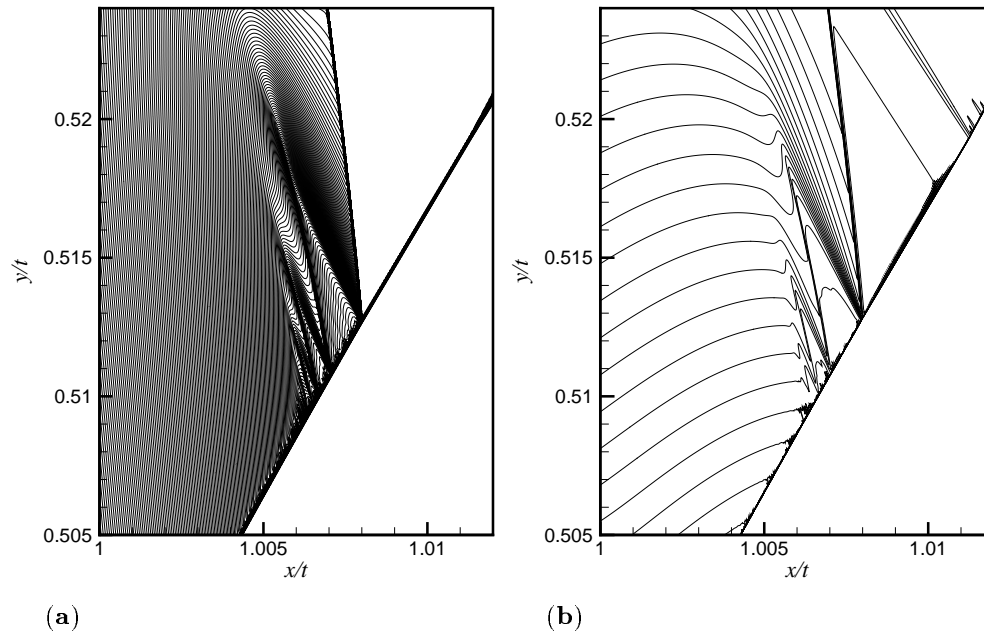
FIG. 5. *A detailed contour plot of (a) u, and (b) v near the triple point for a = 0.5. The u-contour spacing is 0.0005 and the v-contour spacing is 0.001. The sonic line is plotted in Fig. 3(b) and Fig. 6. The figure shows a sequence of shock and expansion waves. Each expansion wave is centered at a triple shock intersection, and reflects off the sonic line into a compression wave. The compression wave forms a shock wave that intersects the Mach shock, resulting in a sequence of triple points. Three shock-expansion wave pairs and triple points are visible in the plots, with indications of a fourth. The region shown contains the refined uniform grid, which has 768 × 608 grid points.*
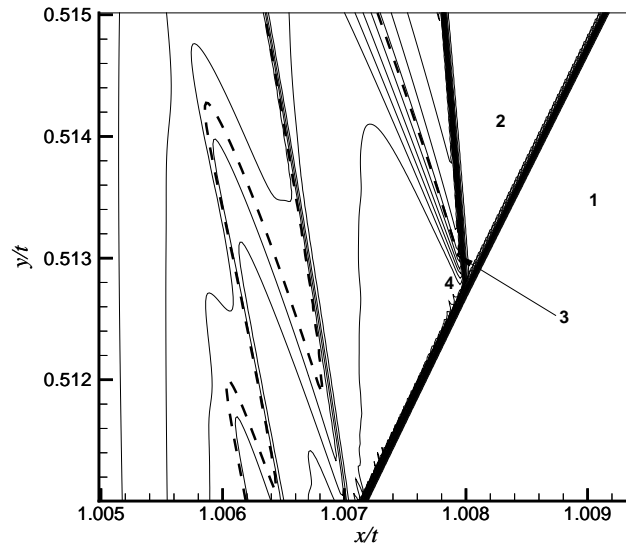
(a)
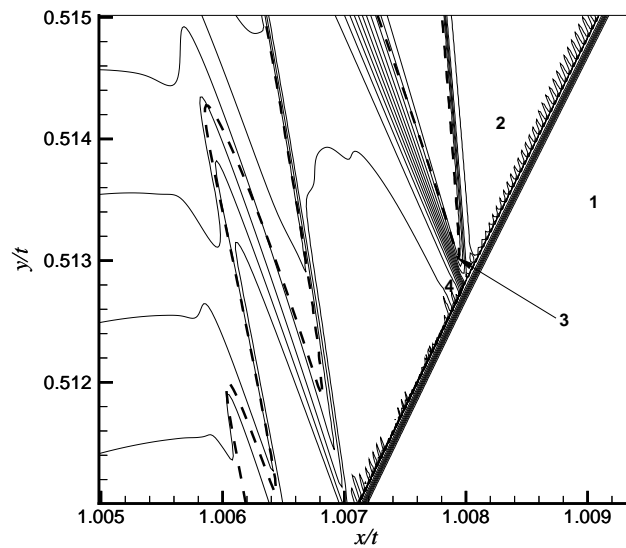
(b)

FIG. 6. *An enlargement of the solution in Fig. 5 near the leading triple point, showing: (a) u-contours; and (b) v-contours. The u-contour spacing is 0.005, and the v-contour spacing is 0.001. The dashed line in the plots is the sonic line. Table 4.2 gives the values of u and v from the numerical solution for the states labeled 1–4 in the plots.*
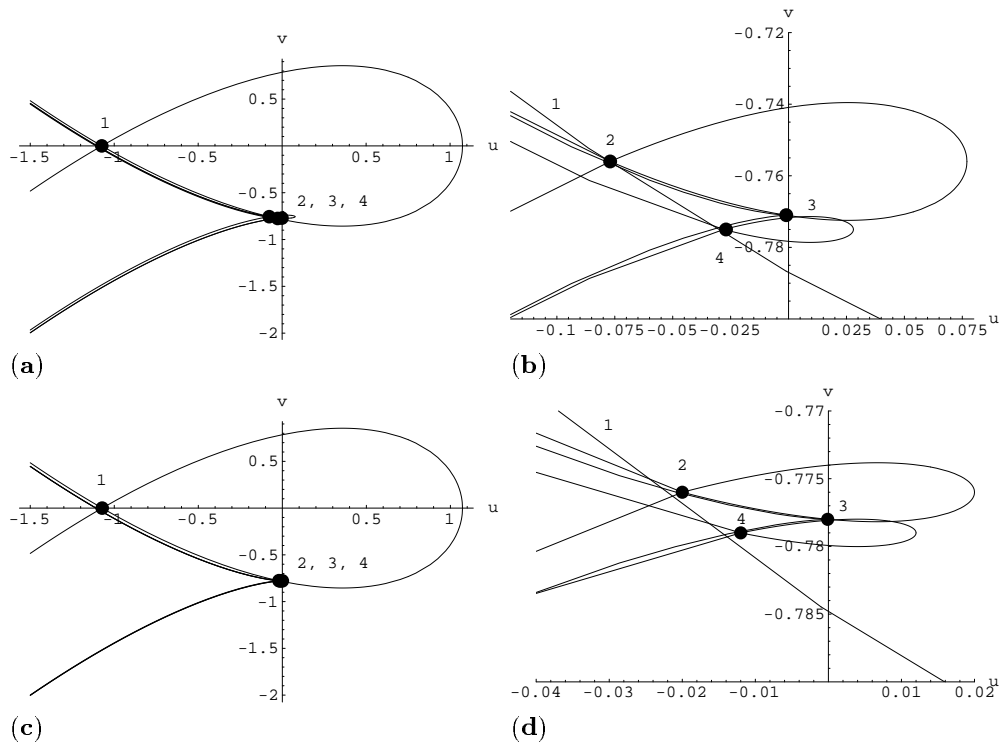
Fig. 7. *The plots in (a)–(b) show the theoretical shock and rarefaction curves through each of the four states for $(\bar{u}, \bar{v})$ at the leading triple point (see Fig. 6). Their numerical values are given in Table 4.2. (The bars have been omitted from the axis labels.) The curves correspond almost exactly to those of a triple point with an expansion fan. The plots in (c)–(d) show similar shock and rarefaction curves for the second triple point. The states 2 and 4 lie slightly off the shock curve of 1; nevertheless, the overall agreement with the curves of a triple point with an expansion fan is excellent.*
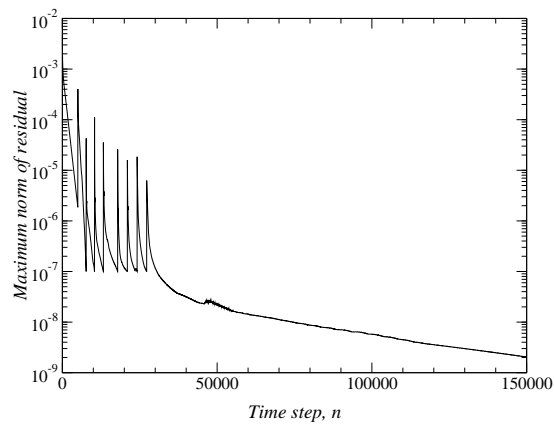
FIG. 8. *A plot of the maximum norm of the residual, showing partial convergence on a sequence of grids, followed by convergence on the most refined grid. The sharp local peaks correspond to interpolations onto more refined grids. The computation on the most refined grid begins at approximately $n = 30000$. The final stage of convergence to a value for the maximum norm of the residual of less than 10^{-9} is not shown in the plot.*
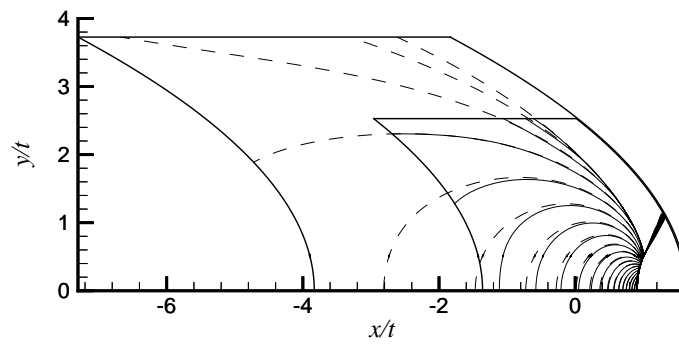
FIG. 9. *A check of the sensitivity of the solutions to the size of the numerical domain, showing u-contours for two solutions computed on different sized domains, for $a = 0.5$. The full numerical domains are shown, with u-contours for the large domain solution (dashed lines) and the small domain solution (solid lines) plotted at the same values of u. Contour lines for u and v near the triple point, for both solutions shown here, are compared in Fig. 10.*
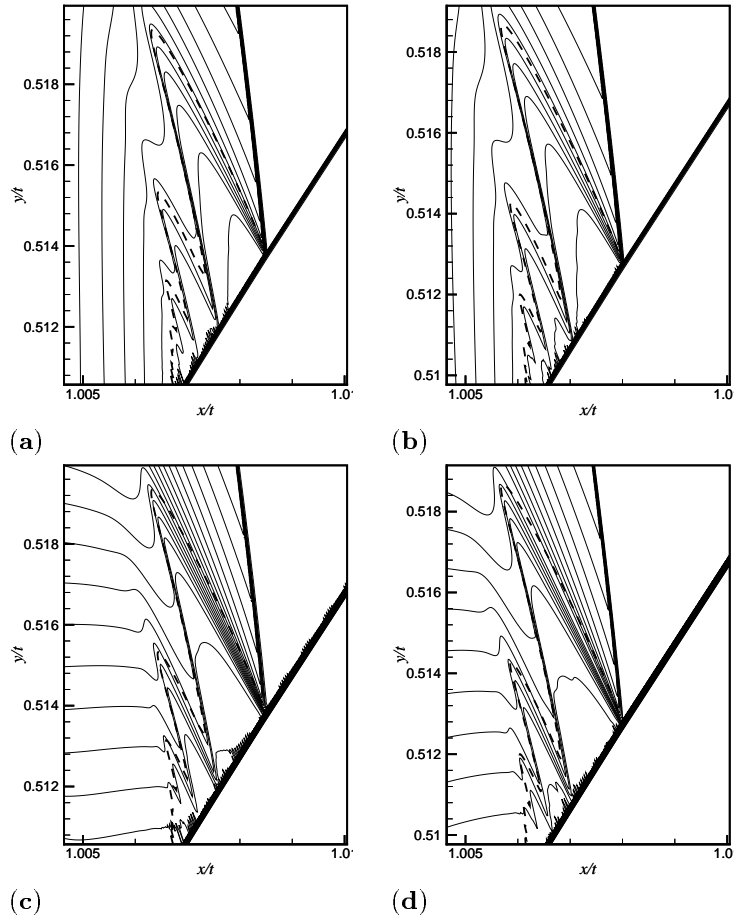
Fig. 10. *A comparison of u and v contours near the triple point, for the two solutions shown in Fig. 9. The plots in (a) and (b) show u-contours for the solutions computed on the larger and smaller domains, respectively, plotted at the same levels of u. The plots in (c) and (d) show v-contours for the solutions computed on the larger and smaller domains, respectively, plotted at the same levels of v. The dashed line in (a)–(d) is the sonic line. The u-contour spacing in (a)–(b) is 0.005, and the v-contour spacing in (c)–(d) is 0.001.*